Seventh International Conference on
Computational Fluid Dynamics (ICCFD7),
Big Island, Hawaii, July 9-13, 2012

ICCFD7-2304

Direct Numerical Simulations of Rayleigh-Taylor instability with gravity reversal

D. Livescu[*] and T. Wei[*]
Corresponding author: livescu@lanl.gov

[*] Los Alamos National Laboratory, NM, USA

Abstract: We present results from an extensive new set of Direct Numerical Simulations (DNS) of Rayleigh-Taylor instability. The set includes a suite of simulations with grid size of $1024^2 \times 4608$ and Atwood number ranging from 0.04 to 0.9, in order to examine small departures from the Boussinesq approximation as well as large density ratio effects, and a high resolution simulation of grid size $4096^2 \times 4032$ and Atwood number of 0.75. After the layer width had developed substantially, additional branched simulations have been run under reversed and zero gravity conditions. These simulations represent unit problems for the variable acceleration case encountered in practical applications. While the bulk of the results will be published elsewhere, here we focus on the modifications in the mixing layer structure and turbulence in response to the acceleration change.

Keywords: Direct Numerical Simulations, Turbulent Mixing, Rayleigh-Taylor instability

1 Introduction

The Rayleigh-Taylor instability (RTI) is generated at the interface between two different density fluids which are subjected to a constant acceleration pointing from the heavy to the light fluid. RTI is of fundamental importance in a multitude of applications ranging from fluidized beds, oceans and atmosphere, to inertial, magnetic, or gravitational confinement fusion, and to most astrophysical explosions [1, 2, 3, 4]. The interface between the two fluids is unstable to any perturbation with a wavelength larger than the cutoff due to surface tension (for the immiscible case) or mass diffusion (for the miscible case). Thus, small perturbations grow to large amplitudes and the interface evolves into bubbles of lighter fluid and spikes of heavier fluid penetrating the opposed fluid. There is a complex phenomenology associated with the evolution of RTI, including formation, competition, and amalgamation of spikes and bubbles, entrainment, and, eventually, turbulence.

Although RTI has been subjected to intense research over the last 50 years, until recently, numerical studies have been restricted to coarse mesh calculations. On the other hand, it is notoriously difficult, in laboratory experiments, to accurately characterize and control the initial conditions and provide the detailed measurements needed for turbulence model development and validation. Thus, a large number of open questions remain unanswered about this instability and even first order global quantities, such as the layer growth, are not completely understood and still give rise to intense debate [5, 6]. Nevertheless, today's petascale computers allow fully resolved simulations of RTI at parameter ranges comparable to those attained in laboratory experiments, but providing, in carefully controlled initial and boundary conditions studies, much more information than physical experiments. These extremely high resolution simulations are enabling a look at the physics of turbulence and turbulent mixing in unprecedented detail, hopefully contributing to a significant advance in our understanding of these phenomena.

The primary nondimensional parameter characterizing differential acceleration effects is the Atwood number, $A = \frac{\rho_2 - \rho_1}{\rho_2 + \rho_1}$, where ρ_1, ρ_2 are densities of the light and heavy fluids, respectively. The Atwood number ranges from 0 to 1. For air inter-penetrating helium, for which the density ratio is $\frac{\rho_2}{\rho_1} \approx 7$, the Atwood number is $A \approx 0.75$. For air and hydrogen, $A = 0.85$. Similar Atwood numbers occur for mixing

between liquid hydrocarbons and air. In contrast, the Boussinesq approximation corresponds to $A \to 0$ and a value of 0.05 is usually taken to define this limit. Most previous numerical studies address the low to moderate A case (e.g. [7, 8, 2, 3, 5]) and to the best of our knowledge the new set of Direct Numerical Simulations (DNS) addressed here is the first to consider $A > 0.5$. Yet, the development of the instability and the mixing itself are fundamentally different at high and low A [5]. For example, our previous results in an idealized triply-periodic buoyancy driven flow show that the mixing is asymmetric at large density ratios, with the pure light and heavy fluids mixing at different rates [9, 10]. At high A, due to the tight coupling between the density and velocity fields, even when the two fluids are incompressible, new cubic nonlinearities arise in addition to the quadratic non-linearities of the incompressible Navier-Stokes equations. Moreover, the velocity field is no longer solenoidal and the specific volume, a function of the amount of each material present, is a new dependent variable. We refer to such flows as variable-density (VD) flows.

Although in many instances, for example in atmospheric or oceanic flows, the acceleration may be considered as constant, there are important practical applications where the driving acceleration changes in time and may even reverse sign. Some examples include ICF, supernovae, or pulsating stars. RTI with complex acceleration history, including changes in sign, have been studied both experimentally and in coarse mesh numerical simulations [11, 12] and references therein; however, much less is known about the physics of the flow compared to the classical RTI. In addition, most engineering turbulence models can not capture the change in the mixing layer behavior following gravity reversal. In order to better understand the variable acceleration effects on the instability development and turbulence properties, we have proposed two unit problems: reversing or setting the acceleration to zero in the turbulent stage of the classical RTI [13]. The latter is related to the Richtmyer-Meshkov instability, when the two fluids are subjected to an impulsive acceleration, e.g. due to a shock wave.

In this paper, we present preliminary results from an extensive new set of very high resolution Direct Numerical Simulations of Rayleigh-Taylor instability, covering the range of Atwood numbers from 0.04 to 0.9. In particular, one of the simulations, at $A = 0.75$ and grid size $4096^2 \times 4032$, is the largest fully resolved instability simulation performed to date. Some results concerning the base case $A = 0.04$ simulation have been discussed in Ref. [5] and preliminary results from some of the simulations have been presented in Ref. [13]. Here, we focus on three simulations, with $A = 0.75$, representing classical, reversed, and zero gravity RTI cases. Nevertheless, the simulations are still being analyzed and the final results will be published elsewhere.

The paper is organized as follows. Section 2 presents the governing equations and numerical approach. Results concerning the flow development and turbulence structure are discussed in section 3. A summary and concluding remarks are provided in section 4.

2   Governing equations, simulation cases, and numerical method

The simulations addressed here pertain to miscible incompressible materials. Thus, the two pure fluids have constant, but different, microscopic densities. In this case, the specific volume and density of the mixture are related to the microscopic densities, ρ_l, and mass fractions, Y_l, by [4]

$$v = \frac{1}{\rho} = \frac{Y_H}{\rho_H} + \frac{Y_L}{\rho_L} \tag{1}$$

which simply states that the total mass inside a control volume is the sum of the masses of the two fluids. The index $l = H, L$ refers to the pure heavy and light fluids, respectively, and $Y_H + Y_L = 1$. The equations describing the instability development can be derived from the compressible Navier-Stokes equations with full multi-component diffusion by taking the limit $P \to \infty$ which ensures incompressibility (see Ref. [4] for the derivation). The limiting process removes the pressure and temperature gradient effects, so that the diffusion operator becomes Fickian in the resulting incompressible equations. Since no other assumption is imposed, the resulting equations are non-Boussinesq. Thus, the density appears in the momentum equations and the divergence of velocity is not zero; the energy equation as well as the species transport equations lead to a formula for the velocity divergence in terms of the derivatives of the density field.

The variable-density equations have been used in several previous studies [4, 3, 9, 2, 7, 14]. In non-dimensional form, they are:

$$\frac{\partial}{\partial t}\rho + (\rho u_j)_{,j} = 0 \tag{2}$$

$$\frac{\partial}{\partial t}(\rho u_i) + (\rho u_i u_j)_{,j} = -p_{,i} + \tau_{ij,j} + \frac{1}{Fr^2}\rho g_i \tag{3}$$

$$u_{j,j} = -\frac{1}{Re_0 Sc}(ln\rho)_{,jj} \tag{4}$$

The viscous stress is Newtonian with

$$\tau_{ij} = \frac{\rho}{Re_0}[u_{i,j} + u_{j,i} - \frac{2}{3}u_{k,k}\delta_{ij}] \tag{5}$$

Note that Eqs. (2)-(3) are the usual continuity and momentum transport equations for compressible flows. Equations (2)-(4) describe the mixing, at any density ratio, between incompressible materials or compressible materials in low speed, low acceleration flows, when the fluids participating in the mixing maintain quasi-constant microscopic densities. If the densities of the two fluids are commensurate, then the mixture density is close to its average value and Eqns. (2)-(4) lead to the Boussinesq approximation (see Ref. [9] for the derivation).

In Eqns. 2-4, u_i is the velocity in direction i, ρ is the mixture density, and p is the pressure. The nondimensional parameters in equations (2)-(4) are the computational Reynolds number, Re_0, Schmidt number, Sc, and Froude number, Fr:

$$Re_0 = L_0 U_0/\nu_0, \quad Sc = \nu_0/\mathcal{D}, \quad Fr^2 = U_0^2/(gL_0) \tag{6}$$

where U_0 and L_0 are reference velocity and length scales, respectively, g_i are the components of the unit vector in the direction of gravity, $\vec{g} = (0,0,-1)$, and the kinematic viscosity, $\nu_0 = \mu/\rho$, and mass diffusion coefficient, $\mathcal{D}$, are assumed constant. Note that, in general, the dynamic viscosity, μ, is a weaker function of density; the assumption ν_0 constant ensures a uniform Sc throughout the flow. The independent variables are the time t and space variables, x_i. Equations (2)-(4) have periodic boundary conditions in the horizontal direction and slip wall conditions are applied in the direction of gravity.

2.1 Numerical methodology

All simulations presented here were performed with the CFDNS code[15]. For this problem, we used sixth-order compact finite differences [16] in the vertical (non-periodic) direction and spectral differencing in the horizontal (periodic) directions. For first two points near the vertical boundaries, 4th and 5th order schemes, respectively, were used. To account for the difference in accuracy between the compact finite differences scheme and the Fourier differentiation, the grid spacing is 25% smaller in the vertical direction. For this grid size, in an incompressible isotropic homogeneous turbulence simulation, the error at the Kolmogorov microscale, η, is around 1% for the compact method, when ηk_{max} is maintained above 1.5 [17]. Nevertheless, since the Kolmogorov microscale is not well defined for the flow considered here, resolution studies were performed to verify that the solution was converged.

The time integration was performed with a third order predictor-corrector Adams-Bashforth-Moulton scheme coupled with a pressure projection method, similar to Refs. [2, 7]. The main difference is how the pressure equation was handled. The variable density equations lead to a variable coefficient Poisson equation for pressure, as shown in Ref. [9]:

$$\nabla \cdot \left(\frac{\nabla P}{\rho^{n+1}}\right) = -\Delta + \nabla \cdot \left[(\rho\vec{u})^*/\rho^{n+1}\right] \tag{7}$$

where the divergence of velocity at time step $n+1$, Δ, is calculated based on ρ^{n+1} (4), which is known. $(\rho\vec{u})^*$ denotes the momentum at the intermediate step, after the momentum equations are advanced without the pressure terms. Instead of interpolating the velocity from the previous step to solve the pressure equation, as done in Refs.[2, 7], equation (7) is solved in two steps, to avoid the introduction of errors that are the same order of the interpolation method in both mass conservation and baroclinic production of vorticity. Thus,

the equation can be split into an explicit equation for the gradient component of $\nabla P/\rho$, which is related to mass conservation, and an implicit equation for the solenoidal (curl) component of $\nabla P/\rho$, which is related to the baroclinic term in the vorticity equation [9, 14].

First, the gradient component of $\nabla P/\rho$ (denoted by ∇q) is determined from:

$$\nabla^2 q = -\Delta + \nabla \cdot \left[(\rho\vec{u})^*/\rho^{n+1}\right] \text{ with } \nabla q \cdot \vec{n}_\Gamma = \left[(\rho\vec{u})^*/\rho^{n+1}\right] \cdot \vec{n}_\Gamma \tag{8}$$

Here, $\vec{n}_\Gamma$ is the normal to the non-periodic boundary, which is in the vertical direction. After applying the Fourier transform in the horizontal directions, equation (8) becomes a second order ordinary differential equation, with Neumann boundary conditions. The equation is discretized using the compact finite differences formula corresponding to Neumann boundary conditions. This leads to a linear system for the Fourier coefficients of q: penta-diagonal for the sixth order or tridiagonal for the fourth order compact schemes, depending on the parallelization used (see below). At the boundaries, lower order schemes (by 2 compared to the central regions), were used. The linear system is solved using a fast direct solver [18]. Note that, for Neumann boundary conditions, q can only be determined up to an arbitrary constant. Thus, q is set to zero at one of the boundaries and the corresponding equation in the linear system is removed.

An equation for the curl component of $\nabla P/\rho$ (denoted by $\vec{Q}$) can be constructed from the formula:

$$\nabla P = \rho^{n+1}(\nabla q + \vec{Q}) \tag{9}$$

by taking the curl twice to yield:

$$\nabla^2 \vec{Q} = \nabla \times \left[\nabla ln\rho^{n+1} \times \left(\nabla q + \vec{Q}\right)\right] \text{ with } \vec{Q}|_\Gamma = 0 \tag{10}$$

Equation (10) is solved iteratively, using the Poisson equation solver described above, with hybrid Fourier transforms / 6th order compact finite differences used to evaluate the right hand side. Note that, unlike the triply periodic case addressed in Refs. [9, 14], a separate equation for the average of $\nabla P/\rho$ is not necessary. This average is included in the gradient component.

The solution algorithm is parallelized using a 3-D domain decomposition. In the vertical direction, the 6th order compact finite differences formula leads to a tri-diagonal system. We have derived a fully distributed algorithm for the corresponding fast direct solver [18]. However, the inversion required by the Poisson equation solver leads to a penta-diagonal system. In this case, depending on the computer architecture, we can use a 4th order scheme for the Laplacian, which still leads to a tri-diagonal system after inversion, or use a serial penta-diagonal direct solver coupled with matrix transposes to arrange the data on an entire line to be on-processor. The same matrix transposes are also used for the Fourier transforms. Usually, such transposes are performed through a "slab" decomposition, and require global all-to-all communications. Nevertheless, the parallel efficiency can be vastly improved by using 1-D matrix transforms (associated with the 3-D domain decomposition) which require communications only in the direction of the transform (or derivative) on single lines of processors.

In all simulations, $Sc = 1$ and the Froude number is chosen such that the mesh Grashoff number, $Gr \equiv 2Ag\Delta_h^3/\nu_0^2 = 2A/Fr^2$, is below 1 (a value of 0.88 was used in simulations). Here $\Delta_h = 1$ is the mesh size in the horizontal direction and the mesh size in the vertical direction is $\Delta_v = 0.8$. In order to ensure the accuracy of the numerical solution, extensive resolution studies have been performed.

The density is initialized to follow an error function profile in the vertical direction, which is consistent to the solution to the pure diffusion equation:

$$\rho = 0.5\left(1 + Erf\left[Y_v z + \zeta(x,y)\right]\right)(\rho_H - \rho_L) + \rho_L, \tag{11}$$

with the slope coefficient Y_v chosen such that 8 grid points lie across the initial mixing layer.

2.2 Nomenclature

In defining the turbulence quantities, capital roman letters, overbars, and angle brackets are used to denote Reynolds averages, which are taken over the periodic directions (assumed homogeneous). Angle brackets are preferred for longer expressions while overbars are used for quantities named with Greek letters. Lower case letters (Roman or Greek) or primes are used to denote fluctuations. The density weighted (Favre) averages,

denoted with ˜, and the corresponding fluctuations with double primes. Thus, the instantaneous velocity, density, pressure, and specific volume are decomposed as $u_i^* = U_i + u_i = \tilde{U}_i + u_i''$, $\rho^* = \bar{\rho} + \rho$, $p^* = P + p$, and $v^* = V + v$, respectively. Note that $\tilde{U}_i - U_i = u_i - u_i'' = a_i$. The definitions for the normalized mass flux, a_i, Favre Reynolds stresses, R_{ij}, and turbulent kinetic energy, $\tilde{k}$, total kinetic energy, E_K, and density specific volume covariance, b, are given below:

$$a_i = \frac{\langle u_i \rho \rangle}{\bar{\rho}} = -\langle u_i'' \rangle \tag{12}$$

$$R_{ij} = \langle \rho^* u_i'' u_j'' \rangle = \bar{\rho} \langle u_i u_j \rangle - \bar{\rho} a_i a_j + \langle \rho u_i u_j \rangle, \tag{13}$$

$$\tilde{k} = R_{kk}/(2\bar{\rho}) = (\langle u_i u_i \rangle - a_i a_i + \langle \rho u_i u_i \rangle / \bar{\rho})/2 \tag{14}$$

$$E_K = \langle \rho^* u_i^* u_i^* \rangle / 2 = (\bar{\rho} \langle u_i u_i \rangle + \langle \rho u_i u_i \rangle)/2 = \bar{\rho}(\tilde{k} + \tilde{K}) \tag{15}$$

$$b = -\langle \rho v \rangle. \tag{16}$$

These quantities are encountered in moment closures (see Ref. [3]) and are useful for the turbulence discussion below.

2.3   Simulation cases

To test various hypotheses related to the layer growth and elucidate the long-standing discrepancy between the experimentally and numerically measured growth rates, explore the turbulence and mixing characteristics, and provide data for model development and testing, we have performed fully resolved, very high resolution simulations of Rayleigh-Taylor instability with the CFDNS code [15]. Most simulations have a grid size of $1024^2 \times 4608$ and cover the range of Atwood numbers, $A = 0.04 - 0.9$, in order to study small departures from the Boussinesq approximation as well as large Atwood number effects. We have also performed a very high resolution simulation with a grid size of $4096^2 \times 4032$ (figure 1) with $A = 0.75$. After the layer width had developed substantially, additional branched simulations have been run under reversed and zero gravity conditions, at A values of 0.04, 0.5, 0.75, and 0.9.
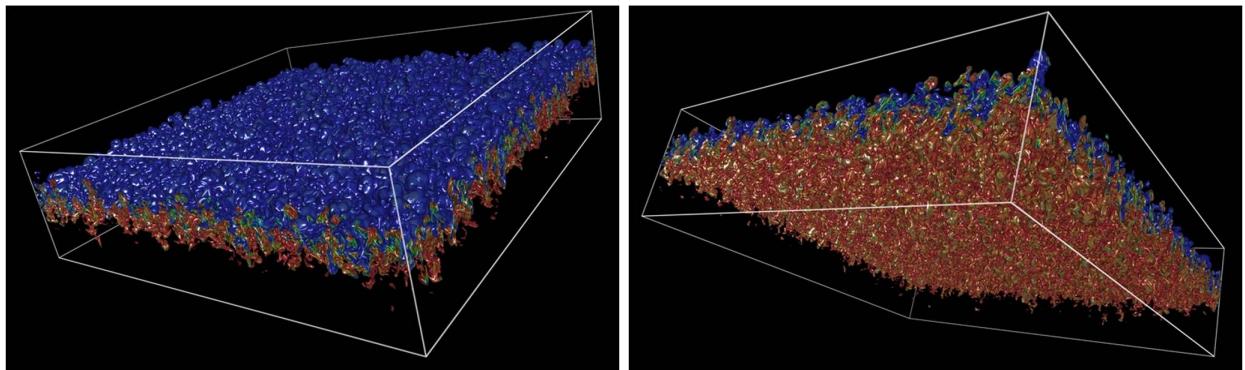

Figure 1: Three-dimensional visualization of the density field at early time, viewed from a) top and b) bottom, showing the asymmetry of the Rayleigh-Taylor mixing layer at $A = 0.75$, with the development of "bubbles" on the heavy fluid side and "spikes" on the light fluid side. From the $4096^2 \times 4032$ simulation.

3   Results pertaining to the reversed and zero gravity cases

In this paper, we mainly discuss results from three simulations, with $A = 0.75$, corresponding to the forward, reversed, and zero gravity cases. The simulations are branched after the forward gravity run has reached the self-similar regime. Most of the results presented below compare the three simulations at the same instant (called hereafter "reference time"), some time after the branching. We also show results at a later instant (called hereafter "late time") to discuss the late time effects of the gravity change. The late instant for

the reversed gravity simulation occurs later, in numerical time, than that corresponding to the zero gravity simulations.

3.1 Overview of flow evolution

The global behavior of the layer after the gravity change can be inferred from figure 2, which shows the evolution of the layer width and maximum turbulent kinetic energy within the layer. After the gravity changes sign, the layer width continues to grow for a short time due to inertia. During this time, as shown below, the layer undergoes dramatic rearrangements of the fluid parcels. As the stratification becomes relatively uniform across the layer, the layer width reaches a quasi-constant value. On the other hand, the zero gravity layer width continues to grow indefinitely, as expected. On the contrary, the turbulent kinetic energy completely reverses its evolution, following the change in gravity. At a later time, there is a slight increase in the kinetic energy for the reversed gravity case, as the local density inversions associated with the complex structure of the layer lead to secondary RT instabilities until the local stratification becomes stable.
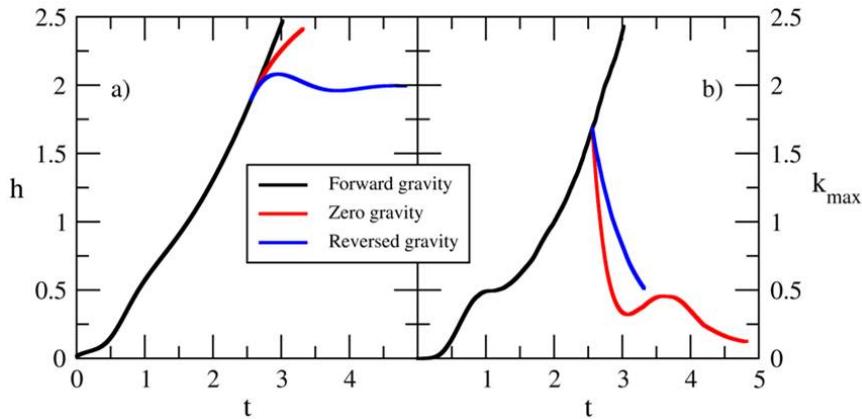

Figure 2: a) Layer width h and b) maximum turbulent kinetic energy across the mixing layer from an $A = 0.75$ simulation. The main simulation (forward gravity) is branched into additional simulations with zero gravity and reversed gravity at time ≈ 2.5.

3.1.1 Density field

The change in the structure of the mixing layer after the gravity reversal can be clearly seen in Figures 3-5. In the forward gravity case, the interpenetration of the two fluids is highly irregular, giving rise to local density inversions, similar to the previous lower A results [3]. These inversions are quickly removed as the buoyancy force reverses sign so that, at late times, the stratification becomes relatively uniform across the layer.

On the contrary, if the gravity is set to zero, the local structures are preserved. As the layer continues to grow due to the inertia of the individual fluid parcels, the instability still develops and the constant density surfaces become even more corrugated. This is similar to the post re-shock evolution of the mixing layer in the Richtmyer-Meshkov instability.

On the other hand, the mean density profiles shown in figure 6 give little indication of the dramatic modifications in the underlying density field structure as the gravity changes. The forward gravity cases results are similar to those obtained at lower A values. After the gravity reverses sign, the mean density steepens slightly; however it shows little variation between the reference and late times. Moreover, the variation remains linear in the inner region of the layer and the edge regions remain asymmetric, with the profiles more elongated on the spike side. The profiles still collapse after the z position is scaled by the layer width (not shown) so that the mean density profiles retain a fixed point at $z = 0$, similar to the classical RTI [3]. As shown in Ref. [3], this leads to a host of asymmetries in many of the turbulence quantities. The
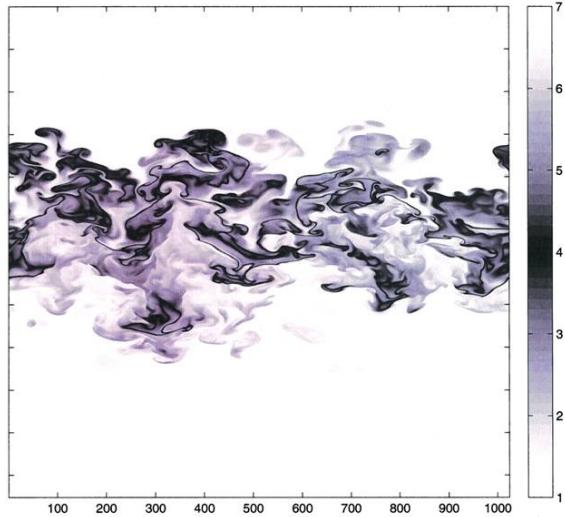
Figure 3: 2-D snapshot of the density field from the forward gravity case at the reference time

collapse of the density profiles is consistent with self-similarity of the layer growth. However, the kinetic energy evolution discussed above is clearly not self-similar and below it is shown that none of the other turbulence quantities analyzed retains the self-similar behavior from the forward gravity case.

In general, all mix metrics in use today for RTI are constructed from lower order moments of the density PDF [5]. Nevertheless, the variation of the density PDF shown in figure 7a) makes clear the limitations in evaluating the molecular mixing based on lower order metrics. Thus, similar to the forward gravity case [5, 13], in the zero gravity case, the density PDF varies widely across the layer: at the top of the layer ($z < 0$) the PDF is spiked at the light fluid, at the bottom is spiked at the heavy fluid, while the transition is non-monotonic. Ref. [10] provides some rigorous bounds on the pure and mixed fluids based on the values of various mix metrics. In many cases, the bounds are far apart, clearly showing that such metrics are not useful in estimating the amounts of pure or mixed fluids. In addition, similar to the forward gravity case, the density PDF at the centerline is not symmetrical, showing that some amount of pure heavy fluid reaches the centerline, but not the pure light fluid. Thus, the penetration distance of the pure heavy fluid is larger than that of the pure light fluid, a consequence of the mixing asymmetry in non-Boussinesq flows [10, 13]. Figure 7b) shows the variation across the layer of the surface density function, Σ, for each density level. Σ profiles are wider at higher z locations, which is towards the light fluid, indicating that at these locations there is a wider range of fluid parcels with different densities. Again, this is a direct consequence of the mixing asymmetry.

After the gravity is reversed, the density PDF as well as the surface density function profiles become much more narrower, with a well defined peak. This is an indication that, at each vertical position, the fluid is well mixed, consistent with the loss of internal structure of the layer seen in the 2-D snapshots.

3.2 Turbulence structure

In this section, some of the flow characteristics related to anisotropy, spectral behavior and vorticity and density gradient alignments are discussed for the three cases considered. These characteristics represent some of the hallmarks of turbulence in the usual canonical turbulent flows. With some notable exceptions, it is shown that the turbulence in the inner region of the mixing layer of all three cases has similar properties with the usual canonical turbulent flows.

3.2.1 Large and small scale anisotropies

In the forward gravity case, it is known that the flow is anisotropic at large scales (e.g. [19, 3, 5]), which is a direct consequence of the anisotropic buoyancy production. The usual measure for this anisotropy is
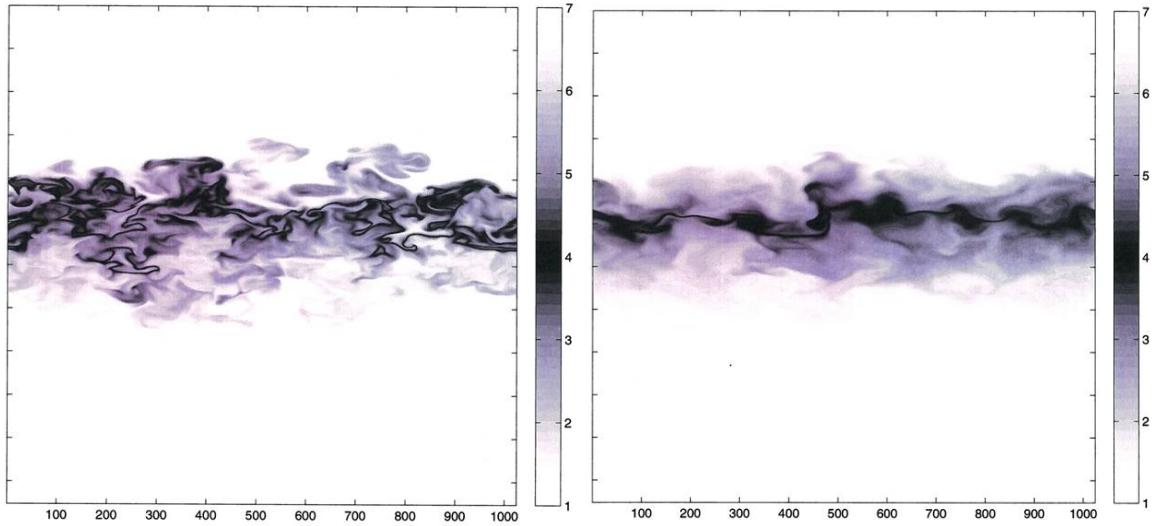
7

Figure 4: 2-D snapshot of the density field from the reversed gravity case at the a) reference time and b) late time.

calculated based on the normal stresses. The Favre Reynolds stress anisotropy tensor is defined by:

$$b_{ij} = \frac{R_{ij}}{R_{kk}} = \frac{1}{3}\delta_{ij} \tag{17}$$

and b_{33} is the relevant large scale anisotropy measure for this flow. b_{33} is bounded by $-\frac{1}{3} \leq b_{33} \leq \frac{2}{3}$. The b_{33} values for the forward gravity case are in the range of those obtained at lower A; however b_{33} is no longer constant across the layer. This is not surprising, since at higher A values it is expected that the asymmetries in the layer become significantly more pronounced. In fact, previous experimental evidence (e.g. [20]) suggests that the high A effects should become evident only for $A > 0.5$. After the gravity is set to zero, the large scale anisotropy decreases considerably, in the absence of the sustained reinforcement of the buoyancy force. Note that the edges of the layer remain more anisotropic than the turbulent interior, as the turbulence is more efficient in mixing the flow. This effect is much more pronounced for the reversed gravity case. The negative acceleration decreases fast the surplus of kinetic energy in vertical direction and helps the mixing in the interior of the layer, so that the anisotropy reduces to zero. However, the edge regions remain slightly more anisotropic than the zero gravity case.

It is generally believed that, in high Reynolds number flows, the small scales become anisotropic and decoupled from the large scales, since, in general, production mechanisms tend to be confined to large scales. However, our previous results [10, 3, 5] show that buoyancy production, even though it becomes much smaller than the nonlinear transfer in the spectral kinetic energy equation at high wavenumbers, has a significant effect on the smallest scales of the flow, in both classical RTI (up tp $A = 0.5$) and an idealized, triply periodic, homogeneous Rayleigh-Taylor flow. If the Reynolds number is large enough, so that the viscous scales are well separated from the large scales, an inertial range can still develop, since buoyancy production decreases faster with the wavenumber than the nonlinear transfer. However, in the viscous range, there is a cancellation between the the two largest terms in the spectral kinetic energy equation and buoyancy production, even though much smaller than these two terms, becomes, again, important. Thus, the largest and smallest scales remain anisotropic. This finding was also confirmed in a stationary, triply periodic buoyancy driven flow [14]. One measure of the anisotropy as a function of scale is $b_{33}(k)$, which is calculated based on the spectral representations of the normal stresses (figure 9). For the forward gravity case, the $b_{33}(k)$ variation remains similar with the lower A results, as expected. In some intermediate range, which would correspond to an emerging inertial range, the anisotropy is much smaller than at large and small scales. For the zero gravity case, the large scale anisotropy decreases somewhat as it does at the end of the spectrum; this is expected for a decaying flow, when the Reynolds number continuously decreases. However, the anisotropy persists in
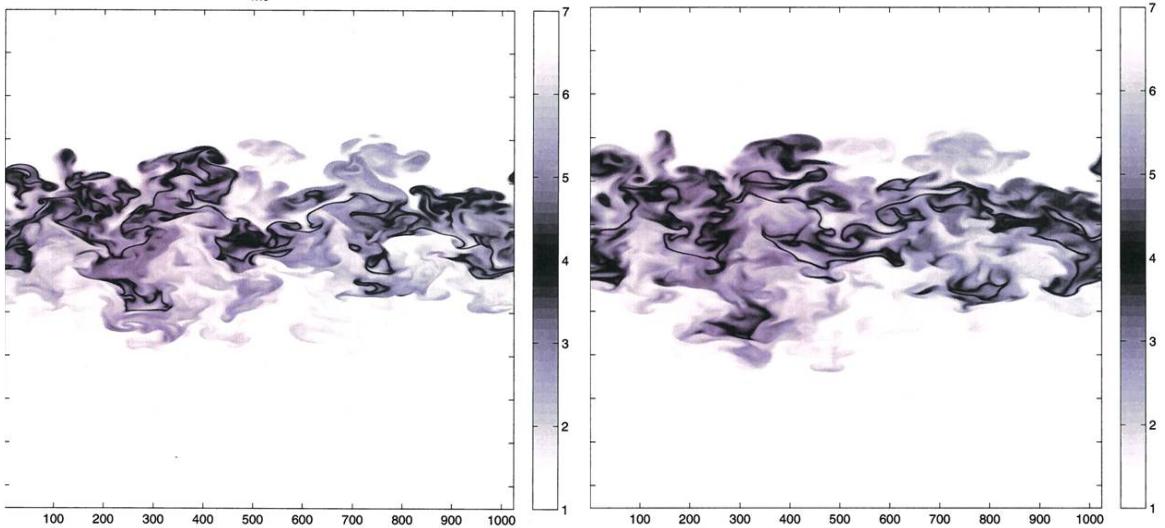
8

Figure 5: 2-D snapshot of the density field from the zero gravity case at the a) reference time and b) late time.
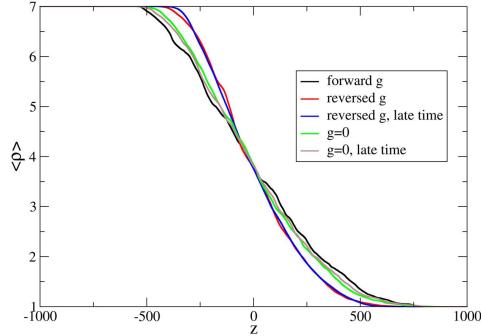

Figure 6: Mean density profiles corresponding to the three cases, at the reference and late times.

the viscous range for both the zero and reversed gravity cases. For the reversed gravity case it seems that the anisotropy is restricted to the smallest scales only. Although reversing gravity represents an efficient mixing mechanism for the large scales, it seems the secondary instabilities generated due to the local density inversions continue to play a significant role in generating small scales turbulence.

3.2.2 Vorticity alignment

In the usual canonical turbulent flows (e.g. homogeneous isotropic incompressible and compressible turbulence), it is known that vorticity tends to align with the β-strain (intermediate) eigenvector of the strain rate tensor, as was first shown in Ref. [21]. The results show that, in the interior of the layer, all three cases are vorticity dominated (as opposed to strain dominance), so that the vorticity still aligns with the β-strain eigenvector. Thus, the PDF of the cosine of the angle with the intermediate eigenvector peaks at 1, indicating a most probable distribution towards a zero degree angle. Interestingly, after the gravity reversal, the secondary instabilities still generate enough vorticity to ensure vorticity dominance (figure 10a). The PDF of the cosine of the angle with the α-strain eigenvector is almost flat, indicating no preference in the alignment. Note that, in the absence of baroclinic generation of vorticity and rotation of the principal axes of the strain rate tensor, vorticity tends to align, exponentially fast, with the α-strain eigenvector. The rotation of the principal axes is the only mechanism preventing this alignment in homogeneous isotropic incompressible turbulence and, therefore an important feature of canonical turbulence. Since there is no preferential
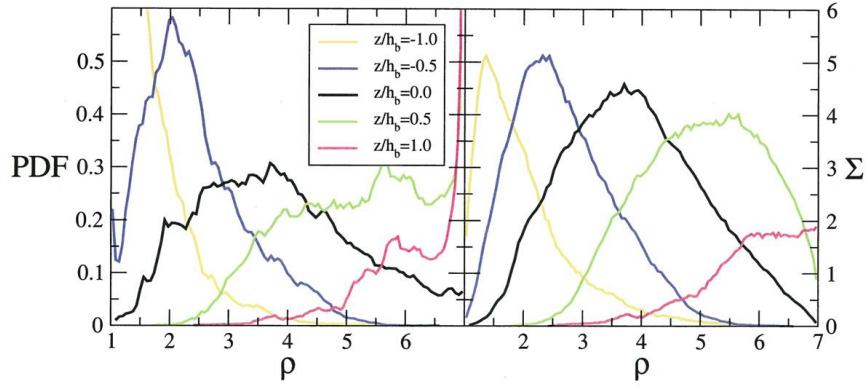
9

Figure 7: a) Density PDF and b) surface density function at several locations across the layer for the zero gravity case at late time.
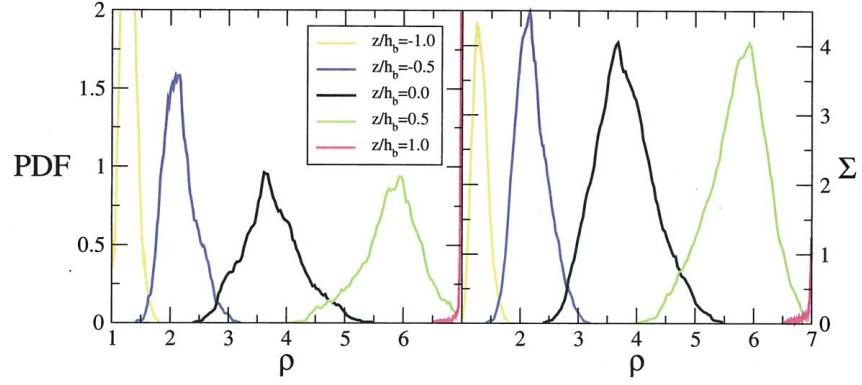

Figure 8: a) Density PDF and b) surface density function at several locations across the layer for the reversed gravity case at late time.

alignment with the α-strain eigenvector, the average of the cosine of the ξ_2 angle should be constant across the layer. Over the non-turbulent edge regions, this alignment changes (not shown here) and $cos\xi_2$ is no longer constant. Thus, the region over which $cos\xi$ is constant can be used as a proxy for the extent of the inner turbulent region of the layer. Figure 10b) shows that this region has about the same extent for the three simulations at the reference time, even though the layer width based on global considerations changes.

3.2.3 Density gradient alignment

The alignment of the density gradient with the eigenvetors of the strain rate tensor is also well studied in canonical turbulent flows. In all instances of isotropic turbulence, the density gradient tends to align with the most compressive (γ)-strain eigenvector. This alignment can be weakened by shear production of turbulence, which is another important turbulence producing mechanism, aside from buoyancy production. In that case, the anisotropic production mechanism also leads to an alignment at an angle different than zero [22]. In all RTI cases considered, the density gradient remains aligned with the γ-strain eigenvector and figure 11 shows that this is also true for the reversed gravity case, at least up to the late time. Since in this case the density gradient is mainly in the vertical direction, this indicates a preferential alignment of the the most compressive eigenvector as well in the vertical direction. Thus, even though the alignment of the density gradient and vorticity with the strain rate tensor eigenvectors remains similar to that seen in canonical turbulence, there is a strong preferential alignment of these quantities with the coordinate directions in the reversed gravity case. Note that, in all other cases, none of these quantities has any preferential alignment with the coordinate directions in the interior of the layer (not shown here); such a preferential alignment is
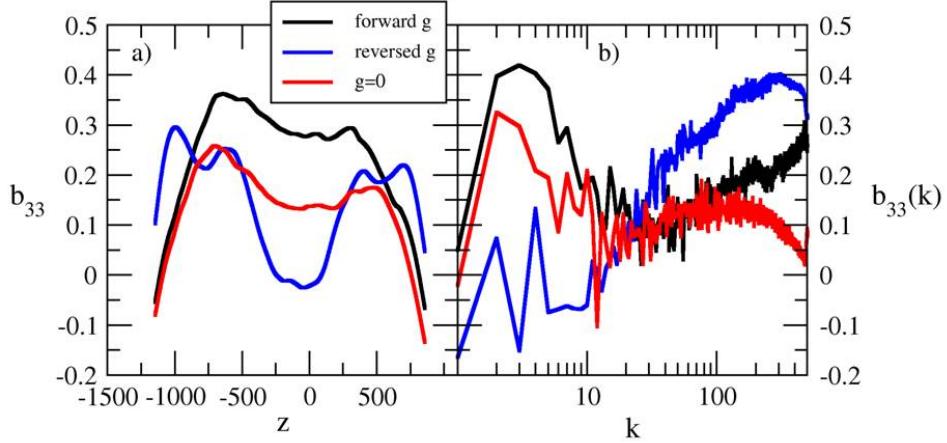
10

Figure 9: a) Vertical variation of b_{33} and b) scale dependence of the normal stresses anisotropy at the centerline, at the reference time.
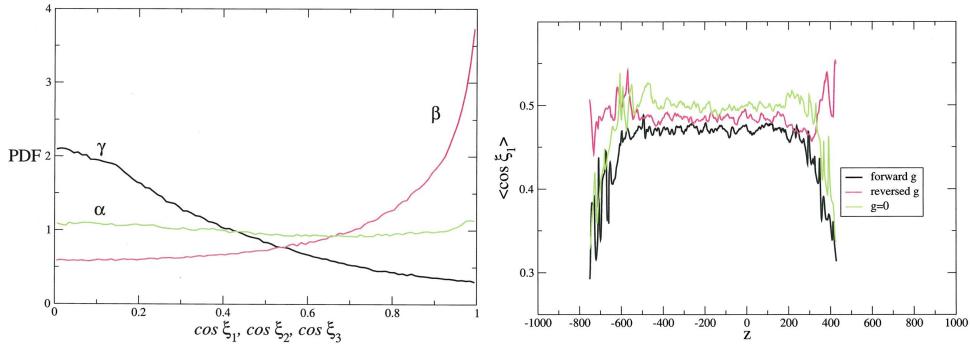

Figure 10: a) PDFs of the cosines of the angles, ξ_1, ξ_2, and ξ_3, between the vorticity vector and the eigenvectors of the strain rate tensor for the reversed gravity case at the reference time. The eigenvectors correspond to the eigenvalues α, β, and γ denoted with the usual convention that $\alpha > \beta > \gamma$. b) Vertical variation of the average of $cos\xi_1$ for the three cases at the reference time.

characteristic to the non-turbulent edges only. Gravity reversal introduces a directionality in the flow which is not restricted to the large scales.

3.3 Modeling issues

A moment closure approach at the second order level requires modeled transport equations for the Favre turbulent kinetic energy, $\tilde{k}$, normalized mass flux, a_i, and density specific volume correlation, b, or, alternatively, mean specific volume, V. The corresponding transport equations can be written as [3, 23]:
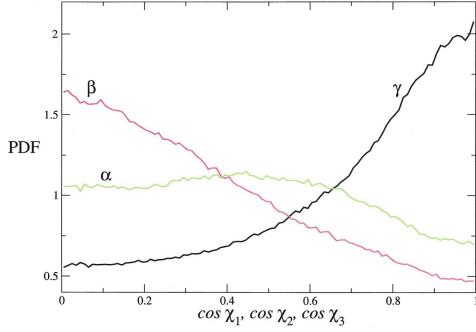
Figure 11: a) PDFs of the cosines of the angles, χ_1, χ_2, and χ_3, between the density gradient and the eigenvectors of the strain rate tensor for the reversed gravity case at the reference time. The eigenvectors correspond to the eigenvalues α, β, and γ denoted with the usual convention that $\alpha > \beta > \gamma$.

$$\frac{\partial}{\partial t}\bar{\rho}\tilde{k} + (\bar{\rho}\tilde{U}_j\tilde{k})_{,j} = a_i(P_{,i} - \bar{t\bar{a}}u_{ij,j}) - R_{ij}\tilde{U}_{i,j} - \frac{1}{2}R_{iij,j}$$
$$- \langle u_i(p\delta_{ij} - \tau_{ij})\rangle_{,j} + \langle pd\rangle - \langle \tau_{ij}u_{i,j}\rangle \tag{18}$$

$$\frac{\partial}{\partial t}(\bar{\rho}a_i) + (\bar{\rho}\tilde{U}_k a_i)_{,k} = bP_i + \bar{\rho}\langle vp_i\rangle - \bar{\rho}a_j(\tilde{u}_i - a_i)_{,j} + \frac{\bar{\rho}_{,j}}{\bar{\rho}}(\langle \rho u_i u_j\rangle - R_{ij})$$
$$+ \bar{\rho}(a_i a_j)_{,j} - (\langle \rho u_i u_j\rangle_{,j} + \bar{\rho}\langle u_i d\rangle) \tag{19}$$

$$\frac{\partial}{\partial t}b + \tilde{U}_j b_{,j} = 2a_j b_{,j} - 2a_j(1+b)\frac{\bar{\rho}_{,j}}{\bar{\rho}} + \bar{\rho}\left(\frac{\langle u_j \rho v\rangle}{\bar{\rho}}\right)_{,j} + 2\bar{\rho}\langle vd\rangle \tag{20}$$

$$\frac{\partial}{\partial t}V + \tilde{U}_j V_{,j} = 2a_j V_{,j} + V\tilde{U}_{j,j} + \left(\frac{\langle u_j \rho v\rangle}{\bar{\rho}}\right)_{,j} + 2\langle vd\rangle \tag{21}$$

The equations above are general and describe the moments evolutions in a fully compressible flow, regardless of the equation of state. Only after the application of (4) they become specific to the VD case.

All the moment equations above contain turbulence transport terms, which are unclosed and important at the edges of the RTI layer [3]. These terms are usually closed using a gradient diffusion hypothesis. In classical RTI, this modeling assumption captures the behavior of the turbulence transport; however, the proportionality coefficient can not be calculated based on the usual turbulence scales before asymptotic self-similarity is approached. To remedy this, it was suggested that a separate lengthscale transport equation, in addition to the one used to model dissipation, is needed [3]. While the data regarding moment closures are still being analyzed following the change in gravity, here we provide some comments regarding the application of the gradient diffusion hypothesis to the mass flux itself. This type of assumption is routinely made in two-equation models of variable density turbulence (e.g. $k - \epsilon$ or $k - L$). Figure 12 shows the variation of the mass flux across the layer for the three cases considered. For the zero gravity case, the mass flux retains a similar behavior across the layer with the forward gravity case, albeit with very different magnitude. However, for the reversed gravity case, the mass flux changes sign at the reference time and becomes very small at the late time. A gradient diffusion hypothesis would model this quantity as being proportional to the mean density gradient. Nevertheless, the mean density gradient does not change much, compared to the forward gravity case, at any of the times shown (see figure 6 above). Thus, a gradient diffusion hypothesis can qualitatively capture the vertical variation of the mass flux, but the proportionality coefficient would need to be significantly modified. This deficiency may be remedied by the introduction of a separate lengthscale transport equation. However, for the reversed gravity case, the mass flux changes sign, while the mean density gradient does not. This change in sign can not be captured by a second lengthscale transport equation and the only possibility within a moment closure strategy for this flow would be to consider a separate mass flux transport equation, as described above. Since similar problems are anticipated for the turbulence transport terms in the additional equation, we are currently investigating avenues for extending

12

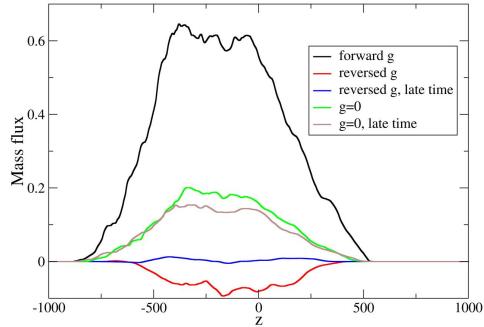moment closure approaches to the reversed gravity case. These results will be published elsewhere.

Figure 12: Mass flux variation across the layer for the three cases, at the reference and late times.

4   Conclusion and Future Work

We have presented preliminary results from high Reynolds number, high resolution Direct Numerical Simulations of Rayleigh-Taylor instability using the CFDNS code [15]. This includes a suite of simulations with Atwood number ranging from 0.04 to 0.9 and grid size of $1024^2 \times 4608$ and a high resolution simulation of grid size $4096^2 \times 4032$ and Atwood number of 0.75. The reference cases have the initial perturbation spectrum as a narrow band around the most unstable mode of the linear problem. After the layer had developed substantially, the simulations have been branched, by reversing gravity and also setting the gravity to zero. In order to study the dependence on initial conditions, we have also performed a multitude of simulations with various initial perturbation spectra, different amplitudes of the initial perturbation, and also with several different values for the molecular viscosity and diffusivity. While the bulk of the results are still being analyzed and will be published elsewhere, here we have presented preliminary results from reversed and zero gravity cases with $A = 0.75$ and compared them with those obtained for the corresponding forward gravity case.

In general, the spectral properties (in terms of fully developed spectra showing the emergence of an inertial range) and vorticity and density gradient alignments with the strain tensor eigenvectors remain similar following the change in gravity with the forward density case and with the usual canonical turbulent flows. However, for the reversed gravity case, the vector quantities enumerated above also acquire a strong directionality with the coordinate directions. In addition, gravity reversal efficiently mixes the large scales in the inner region of the layer, so that the large scales anisotropy decreases to zero and the stratification becomes uniform across the layer. However, the anomalous small scale anisotropy associated to buoyancy driven turbulence is actually increased by gravity reversal.

Moreover, while the mean density profiles do not change much after the change in gravity, the turbulent transport (including the mass flux) changes sign, rendering the popular gradient diffusion hypothesis, used in moment closures, not appropriate. Two-equations models can not capture this flow. Such modifications in behavior following the gravity change are certainly non-trivial. We hope that our new datasets, once fully analyzed, can provide enough insight to reveal new avenues for modeling such flows.

References

[1] D. L. Youngs. Numerical simulation of turbulent mixing by Rayleigh-Taylor instability. *Physica D*, 12:32–44, 1984.

[2] W.H. Cabot and A.W. Cook. Reynolds number effects on Rayleigh-Taylor instability with possible implications for type-ia supernovae. *Nature Phys.*, 2:562–568, 2006.

[3] D. Livescu, J. R. Ristorcelli, R. A. Gore, S. H. Dean, W. H. Cabot, and A. W. Cook. High-Reynolds number Rayleigh-Taylor turbulence. *J. Turbul.*, 10:N13, 2009.

[4] D. Livescu. Numerical simulations of two-fluid turbulent mixing at large density ratios and applications to the Rayleigh-Taylor instability. *to appear in Phil Trans. R. Soc. A*, 2012.

[5] D. Livescu, J. R. Ristorcelli, M. R. Petersen, and R. A. Gore. New phenomena in variable-density Rayleigh–Taylor turbulence. *Phys. Scripta*, T142:014015, 2010.

[6] G. Dimonte and *et al.* A comparative study of the turbulent Rayleigh-Taylor instability using high-resolution three-dimensional numerical simulations: The Alpha-Group collaboration. *Phys. Fluids*, 16:1668–1692, 2004.

[7] A. W. Cook and P. E. Dimotakis. Transition stages of Rayleigh-Taylor instability between miscible fluids. *J. Fluid Mech.*, 443:69–99, 2001.

[8] A. W. Cook, W. H. Cabot, and P. L. Miller. The mixing transition in Rayleigh-Taylor instability. *J. Fluid Mech.*, 511:333–362, 2004.

[9] D. Livescu and J. R. Ristorcelli. Buoyancy-driven variable-density turbulence. *J. Fluid Mech.*, 591:43–71, 2007.

[10] D. Livescu and J. R. Ristorcelli. Variable-density mixing in buoyancy-driven turbulence. *J. Fluid Mech.*, 605:145–180, 2008.

[11] G. Dimonte, P. Ramaprabhu, and M.J. Andrews. Rayleigh-taylor instability with complex acceleration history. *Phys. Rev. E*, 76:046313, 2007.

[12] V.A. Zhmaylo, O.G. Sin'kova, V.N. Sofronov, V.P. Statsenko, Yu.V. Yanilkin, A.R. Guzhova, and A.S. Pavlunin. Numerical study of gravitational turbulent mixing in alternating-sign acceleration. In B. Cheverushkin, A. Ecer, J. Periaux, N. Satufoka, and P. Fox, editors, *Parallel Computational Fluid Dynamics - Advanced Numerical Methods, Software and Applications*, pages 235–241. Elsevier, 2004.

[13] D. Livescu, T. Wei, and M. R. Petersen. Direct Numerical Simulations of Rayleigh-Taylor instability. *J. Phys.: Conf. Ser.*, 318:082007, 2011.

[14] D. Chung and D. I. Pullin. Direct numerical simulation and large-eddy simulation of stationary buoyancy-driven turbulence. *J. Fluid Mech.*, 643:279–308, 2010.

[15] D. Livescu, J. Mohd-Yusof, M. R. Petersen, and J. W Grove. CFDNS: A computer code for direct numerical simulation of turbulent flows. Technical report, Los Alamos National Laboratory, 2009. LA-CC-09-100.

[16] S. K. Lele. Compact Finite Difference Schemes with Spectral-like Resolution. *J. Comp. Phys.*, 103:16–42, November 1992.

[17] M. R. Petersen and D. Livescu. Forcing for statistically stationary compressible isotropic turbulence. *Phys. Fluids*, 22:116101, 2010.

[18] J. Mohd-Yusof, D. Livescu, and T. M. Kelley. Adapting the CFDNS compressible Navier-Stokes solver to the Roadrunner architecture. In R. Biswas, editor, *Parallel Computational Fluid Dynamics, Recent Advances and Future Directions*, pages 95–109. DESTech Publications, 2010.

[19] J.R. Ristorcelli and T.T. Clark. Rayleigh-Taylor turbulence: Self-similar analysis and direct numerical simulations. *LANL Report 03-4273 and J. Fluid Mech.*, 507:213–253, 2004.

[20] G. Dimonte and M. Schneider. Density ratio dependence of Rayleigh-Taylor mixing for sustained and impulsive acceleration histories. *Phys. Fluids*, 12:304–321, 2000.

[21] W.T. Ashurst, A.R. Kerstein, R.M. Kerr, and G.H. Gibson. Alignement of vorticity and scalar gradient with strain rate in simulated navier-stokes turbulence. *Phys. Fluids*, 30:2343, 1987.

[22] D. Livescu and C.K. Madnia. Non-premixed flame-turbulence interaction in compressible turbulent flow. In I.P. Castro, P.E. Hancock, and T.G. Thomas, editors, *Advances in Turbulence IX*. CIMNE, Barcelona, 2002.

[23] J. D. Schwarzkopf, D. Livescu, R. A. Gore, R. M. Rauenzahn, and J. R. Ristorcelli. Application of a second-moment closure model to mixing processes involving multi-component miscible fluids. *J. Turbul.*, 12:1–35, 2011.